Evanescent interference patterns for fluorescence microscopy

James R. Abney,* Bethe A. Scalettar,* and Nancy L. Thompson‡
Departments of *Cell Biology & Anatomy and ‡Chemistry, University of North Carolina, Chapel Hill, North Carolina 27599

ABSTRACT The increasing experimental use of total internal reflection/fluorescence photobleaching recovery has motivated a theoretical study of the spatial intensity profiles generated by two interfering evanescent waves. The interference patterns generated by evanescent waves differ considerably from those generated by plane waves in a homogenous medium because evanescent waves are not transverse and because the evanescent propagation number depends on the incidence angle of the totally internally reflected light. The periodicity and contrast of the evanescent interference patterns under various conditions are calculated; these parameters depend on the intensities, polarizations, and incidence angles of the two incident beams, as well as the refractive indices of the two media that form the planar interface where total internal reflection occurs. The derived intensity profiles are used to develop expressions for the shapes of fluorescence photobleaching recovery curves when evanescent interference patterns are used for fluorescence excitation and bleaching. The calculations also suggest that colliding beam experiments may confirm theoretically predicted evanescent field polarizations.

INTRODUCTION

Total internal reflection (TIR) fluorescence microscopy is a recently developed method for probing molecular and cellular phenomena at fluid/solid interfaces (1–3). In this technique, light is directed from a medium of higher refractive index n_1 (e.g., fused quartz with $n_1 \approx 1.5$) onto a planar interface with a medium of lower refractive index n_2 (usually buffered water with $n_2 \approx 1.3$). For sufficiently oblique incidence angles, the incident light is totally internally reflected at the interface, thereby creating an evanescent electromagnetic field that penetrates only a short distance ($<1{,}000$ Å) into the medium of lower refractive index. This evanescent field selectively excites fluorescence only from those molecules in the medium of lower refractive index that are within the field penetration depth, i.e., close to the surface. It is the exclusion of signal from the bulk phase and the unusual polarization properties of the evanescent field that make TIR fluorescence microscopy a useful probe of surface phenomena. Three recent applications of TIR have been to the characterization of cell-substrate contact regions (4, 5), surface binding equilibria (6–11), and surface orientation distributions (12–15).

Evanescent illumination has also been combined with fluorescence photobleaching recovery to probe surface diffusion coefficients and surface binding kinetic rates. At least two different optical geometries have been used. In one geometry (TIR/FPR), a laser beam with a circular Gaussian intensity profile is totally internally reflected, creating an evanescent intensity profile that varies approximately as an elliptical Gaussian in the plane at which the laser beam totally internally reflects (16–20). Contributions to the fluorescence recovery that arise from surface diffusion for this illumination pattern depend on the $1/e^2$-widths of the elliptical Gaussian intensity profile. In another geometry (TIR/FPPR), two totally internally reflected laser beams collide to create a periodic evanescent interference pattern (21–23). Here contributions to fluorescence recovery that arise from surface diffusion depend on the spatial periodicity of the interference pattern. This latter optical configuration is advantageous because the characteristic length of the illuminated region may be more accurately controlled (by varying the collision angle) and because slower translational motions may be more easily monitored (since the characteristic distance of the illumination is smaller for interference patterns [0.2–5 μm] than for focused Gaussian beams [10–100 μm]).

Despite the fact that TIR/FPPR has been exploited experimentally in several recent applications, the theoretical foundation of the method has not yet been fully developed. This paper describes the evanescent electric field intensities created by two interfering evanescent waves and applies the results to an analysis of TIR/FPPR. It is shown that evanescent interference patterns

Dr. Abney's present address is Cardiovascular Research Institute, University of California, San Francisco, CA 94143-0532.
Dr. Scalettar's present address is Department of Biochemistry and Biophysics, University of California, San Francisco, CA 94143-0554.

0006-3495/91/02/542/11 $2.00

have unique characteristics and differ substantially from the interference patterns created by freely propagating plane waves. These unique characteristics are manifest in the derived forms for TIR/FPPR recovery curves and may also provide a basis for experimentally confirming previous theoretical expressions for evanescent field polarizations.

Plane-wave interference in a homogeneous medium

In this section, the interference patterns created by two colliding plane waves are reviewed. This case is considered because it more simply reveals many of the salient features of the rather complicated evanescent-wave calculation. In addition, the plane-wave results provide a standard against which evanescent-wave interference patterns can be compared.

The electric field of a single plane wave traveling along the x-axis and polarized at an angle α from the z-axis may be written

$$\vec{\mathbf{E}}(\vec{\mathbf{r}}, t) = Re\{A\hat{\mathbf{E}}_0 \exp[i(kx - \omega t)]\}, \quad (1)$$

where $\vec{\mathbf{r}} = (x, y, z)$ is the position, t is the time, A is the amplitude, $\hat{\mathbf{E}}_0$ is a polarization vector of unit amplitude, k is the propagation number, and ω is the angular frequency. The last three quantities are given by the expressions

$$\hat{\mathbf{E}}_0 = \sin\alpha\hat{\mathbf{y}} + \cos\alpha\hat{\mathbf{z}} \quad (2a)$$

$$k = 2\pi n_2/\lambda_0 \quad (2b)$$

$$\omega = 2\pi c/\lambda_0, \quad (2c)$$

where α is the polar angle of the polarization vector, λ_0 is the vacuum wavelength, c is the vacuum speed of light, n_2 is the refractive index of the medium in which the plane wave propagates, and $\hat{\mathbf{y}}$ and $\hat{\mathbf{z}}$ are unit vectors.

Interference phenomena arise from the superposition of two electric fields. The electric fields of two colliding plane waves ($j = 1$ or 2) propagating in the x-y plane at angles $\pm\phi$ from the x-axis, with propagation vectors $\vec{\mathbf{k}}_j$ and $\vec{\mathbf{k}}_2$ and with polarization directions $\hat{\mathbf{F}}_{0j}$ (Fig. 1 *a*), are given by

$$\vec{\mathbf{E}}_j(\vec{\mathbf{r}}, t) = Re\{A_j\hat{\mathbf{F}}_{0j} \exp[i(\vec{\mathbf{k}}_j \cdot \vec{\mathbf{r}} - \omega t + \delta_j)]\}, \quad (3)$$

where

$$\hat{\mathbf{F}}_{01} = -\sin\alpha_1 \sin\phi\hat{\mathbf{x}} + \sin\alpha_1 \cos\phi\hat{\mathbf{y}} + \cos\alpha_1\hat{\mathbf{z}} \quad (4a)$$

$$\hat{\mathbf{F}}_{02} = \sin\alpha_2 \sin\phi\hat{\mathbf{x}} + \sin\alpha_2 \cos\phi\hat{\mathbf{y}} + \cos\alpha_2\hat{\mathbf{z}} \quad (4b)$$

$$\vec{\mathbf{k}}_1 = k_1(\cos\phi\hat{\mathbf{x}} + \sin\phi\hat{\mathbf{y}}) \quad (4c)$$

$$\vec{\mathbf{k}}_2 = k_2(\cos\phi\hat{\mathbf{x}} - \sin\phi\hat{\mathbf{y}}). \quad (4d)$$

Here $\hat{\mathbf{x}}$ is a unit vector, the A_j are amplitudes, and the δ_j have been introduced as arbitrary phases. The above choice of propagation directions facilitates subsequent calculations. Because plane waves are transverse, $\vec{\mathbf{k}}_j \cdot \hat{\mathbf{F}}_{0j} = 0$.

One last set of quantitites is introduced to facilitate later comparison with evanescent-wave interference. The planes defined by the z-axis and the $\vec{\mathbf{k}}_j$ are analogues of incidence planes in reflection/transmission phenomena. Thus, the electric-field amplitudes perpendicular and parallel to these planes can be expressed as

$$A_{s_j}(\alpha_j) = A_j \sin\alpha_j \quad (5a)$$

$$A_{p_j}(\alpha_j) = A_j \cos\alpha_j, \quad (5b)$$

respectively, in analogy with s-polarized and p-polarized incident light.

The "interference" of two plane waves is determined by the spatial variation in the time-averaged intensity, $I(\vec{\mathbf{r}})$, associated with the total

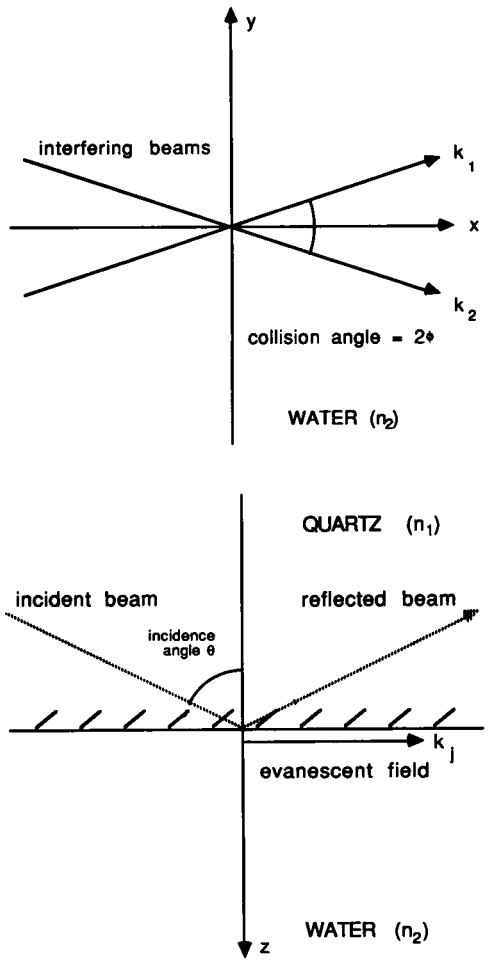

FIGURE 1 Coordinate systems for two interfering evanescent and plane waves. Notation is as follows: (*A*) $\vec{\mathbf{k}}_1$ and $\vec{\mathbf{k}}_2$ are the propagation vectors of the two interfering plane or evanescent-waves; 2ϕ is the collision angle (i.e., the angle between $\vec{\mathbf{k}}_1$ and $\vec{\mathbf{k}}_2$); (*B*) n_1 is the refractive index of the solid in the evanescent wave calculation; and n_2 is the refractive index of the fluid, or medium in which interference occurs, for both evanescent and plane wave calculations. In the case of evanescent interference, θ_j ($j = 1$ or 2) specifies the incidence angle of incident field j, i.e., the angle between the propagation vector of incident field j and the normal to the solid/fluid interface; the incidence plane of wave j is the plane defined by the normal to the solid/fluid interface and the propagation vector of incident wave j. The calculation is simplified by having the x-axis bisect the angle between the two propagation vectors $\vec{\mathbf{k}}_1$ and $\vec{\mathbf{k}}_2$.

electric field[1]

$$\vec{E}_{tot}(\vec{r}, t) = \vec{E}_1(\vec{r}, t) + \vec{E}_2(\vec{r}, t). \quad (6)$$

Thus, the goal is to calculate

$$I(\vec{r}) = \langle \vec{E}^2_{tot}(\vec{r}, t) \rangle \quad (7)$$

where $\langle\ \rangle$ denotes a time average (24). The absorptivity of a randomly oriented sample is proportional to this intensity.

The calculation of $I(\vec{r})$ proceeds by inserting Eq. 3 into Eq. 7 and invoking Eqs. 4 and 5, and the fact that

$$\langle \exp(2i\omega t) \rangle = \langle \exp(-2i\omega t) \rangle = 0 \quad (8)$$

for averaging times much longer than $2\pi/\omega$ (24). The time-averaged intensity is found to be

$$I(\vec{r}) = \tfrac{1}{2}(A^2_{p,1} + A^2_{s,1} + A^2_{p,2} + A^2_{s,2}) + (A_{p,1}A_{p,2} + A_{s,1}A_{s,2} \cos 2\phi) \cos(\Delta\vec{k} \cdot \vec{r} + \Delta\delta), \quad (9)$$

where

$$\Delta\vec{k} = \vec{k}_1 - \vec{k}_2 \quad (10a)$$

$$k_1 = k_2 = k \quad (10b)$$

$$\Delta\delta = \delta_1 - \delta_2. \quad (10c)$$

Eq. 9 is the conventional plane-wave interference pattern (24).

Under typical experimental conditions, Eq. 9 may be simplified. When the amplitudes of the two incident beams are equal and the two beams are either both s-polarized ($A_s \equiv A_{s,1} = A_{s,2}$ and $A_{p,1} = A_{p,2} = 0$) or both p-polarized ($A_p \equiv A_{p,1} = A_{p,2}$ and $A_{s,1} = A_{s,2} = 0$), the intensities equal

$$I_s(\vec{r}) = A^2_s[1 + \cos 2\phi \cos(\Delta\vec{k} \cdot \vec{r} + \Delta\delta)] \quad (11a)$$

$$I_p(\vec{r}) = A^2_p[1 + \cos(\Delta\vec{k} \cdot \vec{r} + \Delta\delta)]. \quad (11b)$$

Evanescent-wave interference at planar dielectric interfaces

In a TIR experiment, a plane wave is directed from a medium (labeled 1) of higher refractive index onto a planar dielectric interface with a medium (labeled 2) of lower refractive index. This wave is totally internally reflected back into the medium of higher refractive index by fixing its incidence angle θ (measured with respect to the interface normal) to be greater than the critical angle θ_c defined by

$$\theta_c = \sin^{-1}(n_2/n_1). \quad (12)$$

Concomitantly, an evanescent field is created in the medium of lower refractive index. If the interface between the two media is defined as the x-y plane and the incidence plane as the x-z plane, the evanescent electric field created by an incident beam of amplitude A that is polarized at an angle α from the incidence plane is (1)

$$\vec{E}(\vec{r}, t) = Re[A\vec{E}_0(\theta, \alpha) \exp[i(k(\theta)x - \omega t)]] \cdot \exp[-z/[2d(\theta)]], \quad (13)$$

where

$$E_{0x}(\theta, \alpha) = a_x(\theta) \cos\alpha \exp[-i[\delta_p(\theta) + \pi/2]] \quad (14a)$$

$$E_{0y}(\theta, \alpha) = a_y(\theta) \sin\alpha \exp[-i\delta_s(\theta)] \quad (14b)$$

$$E_{0z}(\theta, \alpha) = a_z(\theta) \cos\alpha \exp[-i\delta_p(\theta)] \quad (14c)$$

$$a_{x,z}(\theta) = 2\cos\theta X^{-1}(\theta)[(\sin^2\theta - n^2)^{1/2}, \sin\theta] \quad (14d)$$

$$a_y(\theta) = 2\cos\theta/(1 - n^2)^{1/2} \quad (14e)$$

$$X(\theta) = (n^4\cos^2\theta + \sin^2\theta - n^2)^{1/2} \quad (14f)$$

$$\delta_{s,p}(\theta) = \tan^{-1}[(\sin^2\theta - n^2)^{1/2}/([1, n^2]\cos\theta)] \quad (14g)$$

$$d(\theta) = \lambda_0/[4\pi(n_1^2\sin\theta - n_2^2)^{1/2}] \quad (14h)$$

$$k(\theta) = 2\pi n_1 \sin\theta/\lambda_0 \quad (14i)$$

$$n = n_2/n_1. \quad (14j)$$

One noteworthy feature of the evanescent field is that it is not transverse, i.e., $\vec{E}_0$ has a component along the propagation direction (x). However, this component is proportional to a_x, which is much smaller than a_y and a_z for many incidence angles and relative refractive indices. It is also worth noting that the evanescent-wave propagation number (Eq. 14i) depends on the incidence angle; Eq. 14i reduces to Eq. 2b only as $\theta \to \theta_c$.

The analysis of evanescent-wave interference parallels the analysis of plane-wave interference in the previous section. The electric fields of two colliding evanescent waves ($j = 1$ or 2) created by beams with amplitudes A_j, polarization angles α_j, and incidence angles θ_j incident in planes at angles $\pm\phi$ from the x-axis (Fig. 1 *b*) can be written

$$\vec{E}_j(\vec{r}, t) = Re[A_j\vec{F}_{0j}(\theta_j, \alpha_j) \exp[i[\vec{k}_j(\theta_j) \cdot \vec{r} - \omega t + \delta_j]]] \cdot \exp[-z/[2d(\theta_j)]], \quad (15)$$

where

$$\vec{F}_{01}(\theta_1, \alpha_1) = [E_{0x}(\theta_1, \alpha_1)\cos\phi - E_{0y}(\theta_1, \alpha_1)\sin\phi]\hat{x} + [E_{0x}(\theta_1, \alpha_1)\sin\phi + E_{0y}(\theta_1, \alpha_1)\cos\phi]\hat{y} + E_{0z}(\theta_1, \alpha_1)\hat{z} \quad (16a)$$

$$\vec{F}_{02}(\theta_2, \alpha_2) = [E_{0x}(\theta_2, \alpha_2)\cos\phi + E_{0y}(\theta_2, \alpha_2)\sin\phi]\hat{x} + [-E_{0x}(\theta_2, \alpha_2)\sin\phi + E_{0y}(\theta_2, \alpha_2)\cos\phi]\hat{y} + E_{0z}(\theta_2, \alpha_2)\hat{z} \quad (16b)$$

$$\vec{k}_1(\theta_1) = k(\theta_1)(\cos\phi\hat{x} + \sin\phi\hat{y}) \quad (16c)$$

$$\vec{k}_2(\theta_2) = k(\theta_2)(\cos\phi\hat{x} - \sin\phi\hat{y}). \quad (16d)$$

Here $k(\theta_j)$, $\vec{E}_0(\theta_j, \alpha_j)$ and $d(\theta_j)$ are given by Eq. 14 evaluated at θ_j and α_j. Using Eqs. 13–16 in Eqs. 6 and 7, together with the relationships in Eq. 8, gives the following general expression for the time-averaged

[1]The absorptivity of a randomly oriented sample is proportional to the square of the electric field. For plane waves, this quantity is proportional to the energy density given by the Poynting vector. However, for evanescent waves, this proportionality no longer holds because the waves are not transverse (1, 24).

intensity of the evanescent interference pattern[1]

$$I(\vec{r}) = \tfrac{1}{2}\{A_{p,1}^2[a_x^2(\theta_1) + a_z^2(\theta_1)] + A_{s,1}^2 a_y^2(\theta_1)\} \exp(-z/d_1)$$
$$+ \tfrac{1}{2}\{A_{p,2}^2[a_x^2(\theta_2) + a_z^2(\theta_2)] + A_{s,2}^2 a_y^2(\theta_2)\} \exp(-z/d_2)$$
$$+ \{A_{p,1}A_{p,2}[a_x(\theta_1)a_x(\theta_2)\cos 2\phi + a_z(\theta_1)a_z(\theta_2)]$$
$$\cdot \cos(\Delta\vec{k}\cdot\vec{r} + \delta_p(\theta_2) - \delta_p(\theta_1) + \Delta\delta)$$
$$+ A_{s,1}A_{s,2}a_y(\theta_1)a_y(\theta_2)\cos 2\phi$$
$$\cdot \cos(\Delta\vec{k}\cdot\vec{r} + \delta_s(\theta_2) - \delta_s(\theta_1) + \Delta\delta)$$
$$+ A_{s,1}A_{p,2}a_y(\theta_1)a_x(\theta_2)\sin 2\phi$$
$$\cdot \sin(\Delta\vec{k}\cdot\vec{r} + \delta_p(\theta_2) - \delta_s(\theta_1) + \Delta\delta)$$
$$+ A_{p,1}A_{s,2}a_x(\theta_1)a_y(\theta_2)\sin 2\phi$$
$$\cdot \sin(\Delta\vec{k}\cdot\vec{r} + \delta_s(\theta_2) - \delta_p(\theta_1) + \Delta\delta)\} \exp(-z/d_{12}),$$

where $\Delta\vec{k}$ and $\Delta\delta$ are given by Eqs. 10a and 10c, respectively, and

$$d_j = d(\theta_j) \tag{18a}$$

$$d_{12} = 2d_1d_2/(d_1 + d_2). \tag{18b}$$

Again, the interference pattern simplifies considerably under typical experimental conditions. In particular, when the amplitudes and incidence angles of the two incident beams are equal and the two beams are either both s-polarized or both p-polarized, the intensities equal

$$I_s(\vec{r}) = A_s^2 a_y^2[1 + \cos 2\phi \cos(\Delta\vec{k}\cdot\vec{r} + \Delta\delta)] \exp(-z/d) \tag{19a}$$

$$I_p(\vec{r}) = A_p^2[(a_x^2 + a_z^2)$$
$$+ (a_x^2 \cos 2\phi + a_z^2)\cos(\Delta\vec{k}\cdot\vec{r} + \Delta\delta)] \exp(-z/d), \tag{19b}$$

where $d = d_1 = d_2$.

Characteristics of interference patterns

Eqs. 9 and 17 are general expressions for the interference patterns generated by two plane waves and two evanescent waves, respectively; typical patterns are illustrated in Fig. 2. In general, the formulae (Eqs. 9 and 17) are rather complex, but four properties of the interference patterns (their periods, visibilities, spatial shapes, and spatially averaged intensities) may be examined to highlight their important features.

Periodicity. Both the plane-wave and evanescent-wave interference patterns are periodic and consist of a series of fringes of higher and lower relative intensity. The

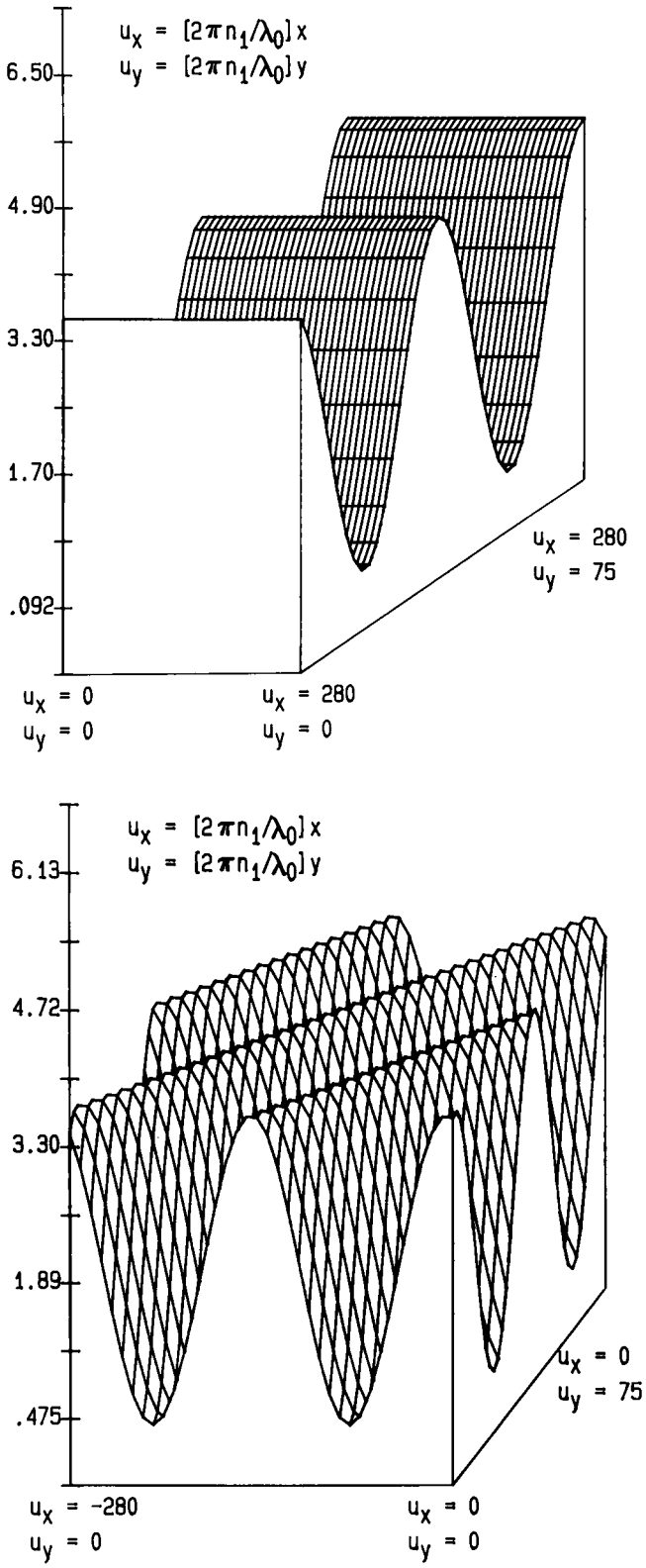

FIGURE 2 Typical interference patterns. The evanescent-wave interference patterns $I(x, y)$ created by p-polarized beams of equal amplitude are shown for (A) $\theta_1 = \theta_2 = 75°$ and $\phi = 5°$ and (B) $\theta_1 = 80°$, $\theta_2 = 70°$, and $\phi = 5°$. The primary features introduced by unequal θ_1 and θ_2 are reduced visibility and a rotation of the pattern. Curves were calculated using Eq. 17 with $z = 0$, $n_1 = 1.467$, $n_2 = 1.334$, and $\Delta\delta = 0°$.

vector period $\vec{\mathbf{P}}$ specifies the distance and direction over which the patterns repeat themselves. The period $\vec{\mathbf{P}}$ can be determined from the expression

$$\Delta\vec{\mathbf{k}} \cdot \vec{\mathbf{P}} = 2\pi \tag{20}$$

as described below.

For interfering plane waves, $k_1 = k_2 = k$, and so it follows (Eqs. 2b, 4cd, and 10b) that

$$\Delta\vec{\mathbf{k}} = (4\pi n_2/\lambda_0) \sin\phi\hat{\mathbf{y}}. \tag{21}$$

The interference pattern is therefore periodic along the y-axis, or perpendicular to the bisector of $\vec{\mathbf{k}}_1$ and $\vec{\mathbf{k}}_2$. Specifically,

$$P_{pw} = (\lambda_0/n_2)/(2 \sin\phi), \tag{22}$$

where λ_0/n_2 is the wavelength of light in a medium with refractive index n_2.

For interfering evanescent waves, the propagation numbers $k(\theta_1)$ and $k(\theta_2)$ are not necessarily equal (Eq. 14i). Thus (Eqs. 10a and 16c,d),

$$\Delta\vec{\mathbf{k}} = [k(\theta_1) - k(\theta_2)] \cos\phi\hat{\mathbf{x}} + [k(\theta_1) + k(\theta_2)] \sin\phi\hat{\mathbf{y}} \tag{23}$$

and the evanescent-wave interference pattern is in general periodic along a direction, $\Delta\vec{\mathbf{k}}$, that is not parallel to $\hat{\mathbf{y}}$. The magnitude of the evanescent-wave period P_{ew} may be obtained by noting that $\vec{\mathbf{P}}_{ew}$ is parallel to $\Delta\vec{\mathbf{k}}$ and then inserting Eqs. 23 and 14i into Eq. 20. The result is

$$P_{ew} = (\lambda_0/n_1)/(\sin^2\theta_1 + \sin^2\theta_2 - 2\sin\theta_1 \sin\theta_2 \cos 2\phi)^{1/2} \tag{24a}$$

$$P_{ew} = (\lambda_0/n_1)/(2 \sin\theta \sin\phi) \quad \text{for } \theta = \theta_1 = \theta_2 \tag{24b}$$

where λ_0/n_1 is the wavelength of light in medium 1.

The plane-wave and evanescent-wave periods are compared in Fig. 3. A rather subtle difference between the two periods is that their magnitudes (Eqs. 22 and 24b) are not in general equal (Fig. 3 *a*). Even if the two evanescent waves are created by beams with equal incidence angles, P_{ew} is smaller than P_{pw} by a factor of $\sin\theta_c/\sin\theta$ (Eq. 12). Nevertheless, for a fixed collision angle, the magnitudes of the periods generally will differ by at most 10% (for a quartz/water interface) and will be equal when $\theta = \theta_c$ (i.e., when the evanescent waves are transverse).

A more striking difference between the periods $\vec{\mathbf{P}}_{ew}$ and $\vec{\mathbf{P}}_{pw}$ is that the former lies along a direction that is rotated about the z-axis by an angle β given by

$$\beta = \cos^{-1}\left[\frac{\sin\phi\,(\sin\theta_1 + \sin\theta_2)}{(\sin^2\theta_1 + \sin^2\theta_2 - 2\sin\theta_1 \sin\theta_2 \cos 2\phi)^{1/2}}\right]. \tag{25}$$

This rotation arises because the evanescent-wave propagation numbers are functions of the incidence angles

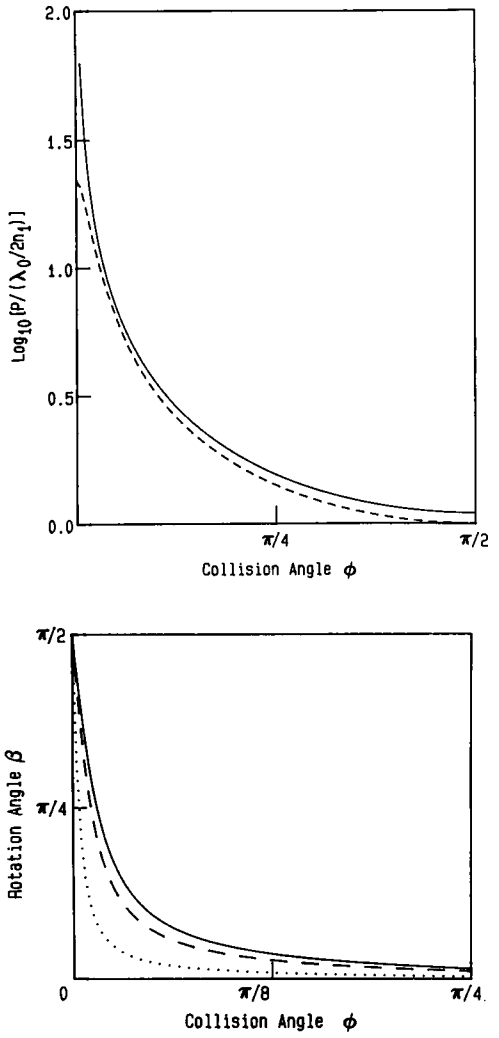

FIGURE 3 Interference pattern periodicities. (*A*) The plane-wave period P_{pw} (Eq. 22) decreases as the collision angle ϕ increases (*solid*). The evanescent-wave period (Eq. 24) is maximized when $\theta_1 = \theta_2 = \theta_c$ (*solid*) and minimized when $\theta_1 = 90°$ and $\theta_2 = \theta_c$, for $2\phi < \cos^{-1}[(1 + n)/2]$, and when $\theta_1 = \theta_2 = 90°$, for $2\phi > \cos^{-1}[(1 + n)/2]$ (*dashed*). (*B*) For equal incidence angles, the rotation angle β (Eq. 25) is zero (not shown). For unequal incidence angles, β approaches 90° when $\phi \to 0$ and 0° when $\phi \to \pi/2$. Curves are shown for $\theta_1 = 90°$ and $\theta_2 = \theta_c$ (*solid*), $\theta_1 = 77.5°$ and $\theta_2 = \theta_c$ (*dashed*), and $\theta_1 = 90°$ and $\theta_2 = 77.5°$ (*dotted*).

(Fig. 3 *b*). However, when the two incidence angles are equal, $\beta = 0$, and the evanescent pattern varies periodically only along the y-axis, just as the plane-wave pattern does. Thus, a possible experimental way to obtain equal incidence angles is to adjust these angles until β is zero.

It is also useful to note the approximate range of values that the plane-wave and evanescent-wave periods can assume under typical experimental conditions. When $n_1 = 1.467$ (quartz), $n_2 = 1.334$ (water), $\lambda_0 = 0.5$ μm, and

$\theta_1 = \theta_2 = 75°$, P_{pw} ranges from 0.187 μm ($\phi = 90°$) to 5.37 μm ($\phi = 2°$) and P_{ew} ranges from 0.176 μm ($\phi = 90°$) to 5.06 μm ($\phi = 2°$).

Finally, the expressions for the periods obtained here differ from those used in previous analyses of evanescent-wave interference experiments. In the past, evanescent-wave interference has been modeled as simple p-polarized plane-wave interference (21–23). Because this approximation is not rigorously correct, it is not surprising that the expressions derived here differ somewhat from those published previously. Nevertheless, the plane-wave approximation will give fairly accurate answers under many experimental conditions.

Visibility. Both interference patterns consist of fringes that alternate spatially between higher and lower relative intensities. The contrast or distinctness of the fringes can be described by the visibility, V, defined as

$$V = \frac{I_{max} - I_{min}}{I_{max} + I_{min}}, \tag{26}$$

where I_{max} and I_{min} are the maximum and minimum intensities (24). The visibility ranges between one and zero and assumes these extreme values when the contrast is maximal ($I_{min} = 0, V = 1$) or minimal ($I_{max} = I_{min}, V = 0$), respectively.

The plane-wave visibility can be determined from Eqs. 26 and 9. Because in general V is a rather complicated function of polarizations, amplitudes, etc., here it is analyzed only for two important special cases. In the first case, both plane waves are s-polarized (i.e., $\alpha_j = 90°$); the intensity is then given by Eq. 11a. The maxima and minima of this function, I_{max} and I_{min}, for a fixed value of ϕ, are attained when the second cosine term in Eq. 11a assumes the values +1 and −1, respectively. Thus, the visibility of the plane-wave interference pattern for s-polarization is given by the relatively simple expression

$$V_s = \frac{2A_{s,1}A_{s,2}|\cos 2\phi|}{A_{s,1}^2 + A_{s,2}^2} \tag{27a}$$

$$V_s = |\cos 2\phi| \quad \text{for } A_{s,1} = A_{s,2}. \tag{27b}$$

In the second case, both plane waves are p-polarized (i.e., $\alpha_j = 0°$). The visibility is then given by

$$V_p = \frac{2A_{p,1}A_{p,2}}{A_{p,1}^2 + A_{p,2}^2} \tag{28a}$$

$$V_p = 1 \quad \text{for } A_{p,1} = A_{p,2}. \tag{28b}$$

Eqs. 27 and 28 show that both visibilities are maximal when the amplitudes A_s and A_p are equal.

The evanescent-wave visibility can be determined from Eqs. 26 and 17 and is a fairly complicated function of the beam polarizations, incidence angles and amplitudes, and the two refractive indices. Also, if the incidence angles are not equal, the visibility depends on the distance from the interface (z). However, the expression for V simplifies considerably if the incident beams are either both s-polarized or both p-polarized. If both incident waves are s-polarized, the visibility V_s is

$$V_s = \frac{2A_{s,1}A_{s,2}|\cos 2\phi|\cos\theta_1 \cos\theta_2 \exp(-z/d_{12})}{A_{s,1}^2 \cos^2\theta_1 \exp(-z/d_1) + A_{s,2}^2 \cos^2\theta_2 \exp(-z/d_2)} \tag{29a}$$

$$V_s = |\cos 2\phi| \quad \text{for } \theta_1 = \theta_2 \quad \text{and} \quad A_{s,1} = A_{s,2}. \tag{29b}$$

If both incident waves are p-polarized, the visibility is

$$V_p = \frac{2X(\theta_1)X(\theta_2)A_{p,1}A_{p,2}\cos\theta_1 \cos\theta_2 |[(\sin^2\theta_1 - n^2) \cdot (\sin^2\theta_2 - n^2)]^{1/2} \cos 2\phi + \sin\theta_1 \sin\theta_2| \exp(-z/d_{12})}{A_{p,1}^2 X^2(\theta_2)\cos^2\theta_1(2\sin^2\theta_1 - n^2)\exp(-z/d_1) + A_{p,2}^2 X^2(\theta_1)\cos^2\theta_2(2\sin^2\theta_2 - n^2)\exp(-z/d_2)} \tag{30a}$$

$$V_p = \frac{(\sin^2\theta - n^2)\cos 2\phi + \sin^2\theta}{2\sin^2\theta - n^2} \quad \text{for } \theta_1 = \theta_2 \quad \text{and} \quad A_{p,1} = A_{p,2}. \tag{30b}$$

The plane-wave and evanescent-wave visibilities are compared in Fig. 4 for the special cases in which the two incident beams are both s-polarized or both p-polarized and the amplitudes and incidence angles are equal. If both beams are s-polarized, the plane-wave and evanes-

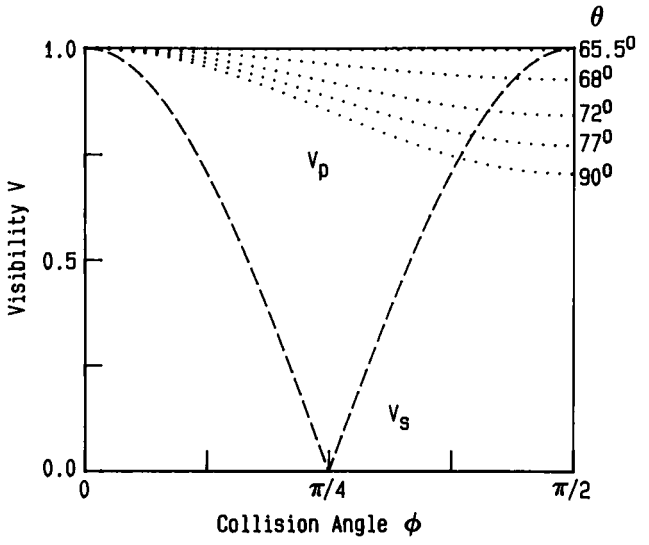

FIGURE 4 Interference pattern visibilities. For beams of equal amplitudes and incidence angles, the plane-wave (Eqs. 27 and 28) and evanescent-wave (Eqs. 29 and 30) visibilities are equal for s-polarized (*dashed*) incident beams but not for p-polarized (*dotted*) incident beams. For p-polarized beams, the visibilities are equal only when the incidence angles θ_j approach the critical angle θ_c. Plots were generated using Eqs. 27b, 28b, 29b, and 30b with $n_1 = 1.467$ and $n_2 = 1.334$.

cent-wave visibilities are equal (Eqs. 27b and 29b). In this case, the visibility varies as $|\cos 2\phi|$ and therefore decreases with increasing collision angle (up to $\phi = \pi/4$). In contrast, if both beams are p-polarized, the plane-wave and evanescent-wave visibilities differ, even if the incidence angles are equal (Eqs. 28b and 30b). The plane-wave visibility equals one for all collision angles, whereas the evanescent-wave visibility is a function of the collision angle and assumes values smaller than one. However, as the incidence angles approach the critical angle θ_c (i.e., as the evanescent waves become transverse), the plane-wave and evanescent-wave visibilities become identical even if the light is p-polarized.

It is also useful to note the magnitude of the plane-wave and evanescent-wave visibilities under typical experimental conditions. When $\phi = 10°$, $\theta = 75°$, and $n = 1.334/1.467$, the plane-wave visibilities are $V_s = 0.94$ and $V_p = 1$, and the evanescent-wave visibilities are $V_s = 0.94$ and $V_p = 0.99$.

Finally, the largest visibilities typically define the most desirable experimental conditions. For s-polarized incident beams and a fixed value of ϕ, the largest visibility is obtained for equal incidence amplitudes and incidence angles. For p-polarized incident beams and a fixed value of ϕ, the largest visibility is obtained for equal incidence amplitudes and both incidence angles equal to θ_c.

Shapes of interference patterns. Although plane-wave interference patterns always vary spatially as a single cosine term (Eq. 9), evanescent-wave interference patterns generally depend on a superposition of several phase-shifted cosine terms (Eq. 17). However, for many experimental conditions, the evanescent-wave patterns also vary as a single cosine. For example, if both beams are either s-polarized or p-polarized, three of the last four terms in Eq. 17 equal zero, and the functional form for the evanescent intensity reduces to a constant plus a cosine term. Also, for many incidence angles and relative refractive indices, $a_x \ll a_y \approx a_z$, and the last two terms in Eq. 17 are therefore negligible. When these terms are small, the evanescent intensity varies as two cosine terms whose difference in phase, $[\delta_s(\theta_2) - \delta_s(\theta_1)] - [\delta_p(\theta_2) - \delta_p(\theta_1)]$, is zero when $\theta_1 = \theta_2$ and is $\leq 3°$ (Eq. 14g) under almost all other experimental conditions.

Spatially averaged intensity. The spatially averaged intensities I^a are given by the spatially independent terms in Eq. 9 and 17, because the spatially dependent terms average to zero. The general expressions for plane-wave (Eq. 31a) and evanescent-wave (Eq. 31b, at $z = 0$) interference are

$$I^a = \tfrac{1}{2}(A_{p,1}^2 + A_{s,1}^2 + A_{p,2}^2 + A_{s,2}^2) \tag{31a}$$

$$I^a = \tfrac{1}{2}[A_{p,1}^2[a_x^2(\theta_1) + a_z^2(\theta_1)] + A_{s,1}^2 a_y^2(\theta_1)] + \tfrac{1}{2}[A_{p,2}^2[a_x^2(\theta_2) + a_z^2(\theta_2)] + A_{s,2}^2 a_y^2(\theta_2)]. \tag{31b}$$

For a quartz/water interface, the factors $[a_x^2(\theta) + a_z^2(\theta)]$ and $a_y^2(\theta)$ range between 5 and 0 for $\theta_c < \theta < 90°$ (1); thus the average evanescent intensity at the interface ($z = 0$) may be several-fold higher than the sum of the intensities of the incident beams.

Application to TIR/FPPR

In recent experimental work, interfering evanescent fields and fluorescence pattern photobleaching recovery have been combined into the technique TIR/FPPR (21–23). In this technique, fluorescent molecules adsorbed to a liquid/solid interface are bleached and probed with an evanescent interference pattern. Fluorescence recovery then occurs as bleached molecules exchange with unbleached molecules by diffusing along the surface or by associating and dissociating from the surface. In this section, the theoretical foundation of TIR/FPPR is developed.

If the surface affinity and site density are high enough, the dominant signal in a TIR/FPPR experiment arises from molecules that are bound to the surface rather than those in solution near the surface (6, 7). In this case, the measured fluorescence will be related to the evanescent intensity at the interface ($z = 0$). For interfering beams with equal incidence angles, amplitudes, and polarizations, this intensity may be written in the form

$$I(y) = I^a[1 + V\cos(2\pi y/P_{ew} + \Delta\delta)], \tag{32}$$

where I^a is the spatially averaged intensity (Eq. 31b), V is the visibility (Eqs. 29b and 30b), and P_{ew} is the period (Eq. 24b).

The time-dependent fluorescence recovery $F(t)$ following photobleaching is approximately equal to

$$F(t) = Q\int_0^{P_{ew}} I(y)C(y,t)\,dy, \tag{33}$$

where Q is a proportionality constant and $C(y,t)$ is the surface concentration of unbleached fluorescent molecules at time t and position y. Eq. 33 assumes that the fluorophore absorption dipoles are isotropically oriented and homogeneously distributed. The equation also neglects the (often small) effects of the nearby planar dielectric interface on the angular dependence of the fluorescence emission and the influence of the microscope collection optics on the fluorescence collection efficiency.

$C(y,t)$ is given by the solution of the appropriate diffusion equation (see below), subject to the initial concentration distribution (25)

$$C(y,0) = \overline{C}\exp[-\kappa I_b(y)] \tag{34a}$$

$$C(y,0) \approx \overline{C}[1 - \kappa I_b(y)] \quad \text{for } \kappa I_b^a \ll 1, \tag{34b}$$

where $I_b(y)$ is the bleaching beam intensity profile, which is assumed to be proportional to Eq. 32. In Eq. 34, κ is a parameter proportional to the bleaching duration and efficiency, and $\overline{C}$ is the total surface density of bleached and unbleached fluorescent molecules. The approximation given in Eq. 34b is valid for low bleaching depths. The prebleach fluorescence $F(-)$ is obtained from Eq. 33 when $C(y, t) = \overline{C}$.

Lateral diffusion. In some samples, fluorescent molecules remain bound to the surface, and the fluorescence recovery results only from lateral diffusion along the interface. Solving the diffusion equation for $C(y, t)$ subject to the initial condition given in Eq. 34a (assuming that mobile and immobile molecules are bleached with equal efficiencies) and inserting $C(y, t)$ into Eq. 33 yields the following normalized fluorescence recovery

$$F(t)/F(-) = \exp(-\eta)\{I_0(\eta V) - VI_1(\eta V) + \gamma V I_1(\eta V)[1 - \exp(-(2\pi/P_{ew})^2 D_s t)]\} \quad (35a)$$

$$F(t)/F(-) = (1 - \eta - \tfrac{1}{2}V^2\eta) + \tfrac{1}{2}V^2\eta\gamma\{1 - \exp[-(2\pi/P_{ew})^2 D_s t]\} \quad \text{for } \eta \ll 1, \quad (35b)$$

where γ is the fraction of the fluorescent molecules that are mobile, D_s is the lateral diffusion coefficient of adsorbed molecules, I_0 and I_1 are modified Bessel functions, and

$$\eta = \kappa I_b^a. \quad (36)$$

When $V = 1$ and $\gamma = 1$, Eq. 35a reduces to a previously published expression obtained for epi-illumination pattern photobleaching with interference fringes (26); when $V = 1$, Eq. 35b reduces to a previously published expression obtained assuming the p-polarized plane-wave approximation for the evanescent-interference illumination pattern (21, 22).

The fractional fluorescence recovery R associated with Eq. 35 is given by

$$R = \frac{[F(\infty) - F(0)]}{[F(-) - F(0)]} = \frac{\gamma V \exp(-\eta) I_1(\eta V)}{1 - \exp(-\eta)[I_0(\eta V) - VI_1(\eta V)]} \quad (37a)$$

$$R = \gamma V^2/(2 + V^2) \quad \text{for } \eta \ll 1. \quad (37b)$$

Fig. 5 shows the general dependence of R on the visibility V and bleaching parameter η when all fluorescent molecules are mobile ($\gamma = 1$). The maximum fractional recovery, $R = \frac{1}{3}$, occurs when $V = \gamma = 1$ and $\eta = 0$. The relatively small fractional recovery will make it somewhat difficult to quantify parameters such as mobile fractions and diffusion coefficients with TIR/FPPR.

The results in Eqs. 35 and 37 differ in at least three ways from the comparable results for FPPR with a square-wave illumination pattern (27) and FPR with Gaussian-shaped evanescent illumination (28). First, for evanescent-interference illumination the temporal dependence of $F(t)$ is monoexponential (Eq. 35), whereas for square-wave and Gaussian-evanescent illumination the temporal dependence of $F(t)$ is determined by an infinite sum of exponential terms and a Lorentzian function, respectively. Second, the maximum fractional recovery is one-third for evanescent-interference illumination (Eq. 37), one-half for square-wave illumination, and one for Gaussian-evanescent illumination. (Fractional recoveries are bleach dependent for evanescent-interference illumination but not for square-wave or Gaussian-evanescent illumination.) Finally, of the three illumination profiles, the smallest characteristic distance scales can be achieved with evanescent-interference illumination, and therefore the slowest diffusion is detectable with TIR/FPPR.

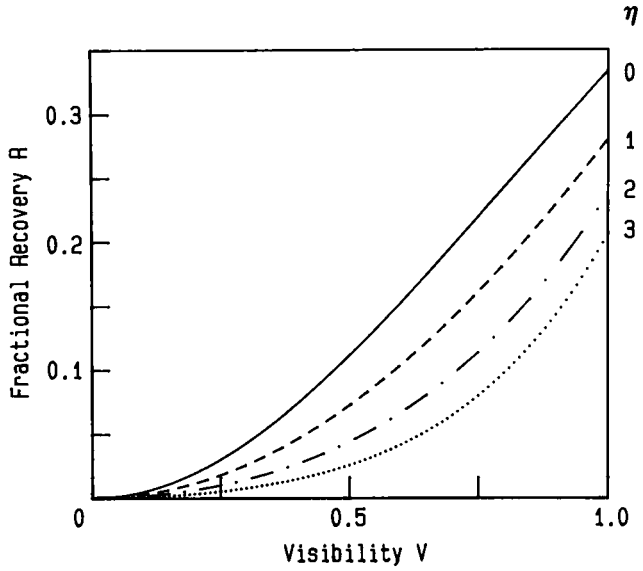

FIGURE 5 TIR/FPPR fractional recoveries. The fractional recovery R for a sample in which all bleached molecules are translationally mobile ($\gamma = 1$) increases with the evanescent-wave visibility V and decreases with the bleaching parameter η. Curves were calculated using Eq. 37a and $\eta \to 0$ ($F(0)/F(-) \to 1$; *solid*), $\eta = 1$ ($F(0)/F(-) = 0.368$; *dashed*), $\eta = 2$ ($F(0)/F(-) = 0.135$; *dot-dash*), and $\eta = 3$ ($F(0)/F(-) = 0.050$; *dotted*).

Lateral diffusion with monovalent surface binding. In some samples, fluorescent molecules are loosely bound and in equilibrium between the solution and the surface. In this case the fluorescence recovery depends in general on the rates of surface and solution diffusion as well as the kinetic rates for surface association and dissociation. Previous work (28) has considered the monovalent

surface reaction

$$A + B \underset{k_{off}}{\overset{k_{on}}{\rightleftharpoons}} C. \tag{38}$$

For this binding mechanism, and in the limit of low bleaching, the shape of the fluorescence recovery is described by

$$F(t) = F(-) + [F(0) - F(-)]g(t) \tag{39a}$$

$$g(t) = \frac{\int |I(\vec{\mathbf{q}})|^2 S(q,t)\, d^2q}{\int |I(\vec{\mathbf{q}})|^2\, d^2q}, \tag{39b}$$

where the integrals are over all two-dimensional space, $I(\vec{\mathbf{q}})$ is the Fourier transform of $I(\vec{\mathbf{r}})$, and $S(q,t)$ is a rather complicated (but analytically known) function that depends on k_{on}, k_{off}, A, D_s, the total surface site density, the solution diffusion coefficient, and the spatial parameters of $I(\vec{\mathbf{r}})$. The function $g(t)$ ranges from one (at $t = 0$) to zero (as $t \to \infty$).

The ability to evaluate Eq. 39b analytically is critically dependent upon the functional form for the illumination pattern. For the spatial intensity profile generated by a totally internally reflected Gaussian-shaped laser beam (an elliptical Gaussian), the complexity of the functional form for $S(q,t)$ dictates that the integral in Eq. 39b be evaluated numerically. This lack of a closed-form solution significantly hinders curve-fitting in the analysis of experimental data. However, for the spatial intensity profile generated by interfering evanescent waves (see Eq. 32)

$$|I(\vec{\mathbf{q}})|^2 \propto \delta(\vec{\mathbf{q}}) + V^2[\delta(\vec{\mathbf{q}} + 2\pi\hat{\mathbf{y}}/P_{ew}) + \delta(\vec{\mathbf{q}} - 2\pi\hat{\mathbf{y}}/P_{ew})]/4, \tag{40}$$

where the $\delta(\,)$ are Dirac delta functions. Therefore, in this latter case, the integral in Eq. 39b can be evaluated analytically, yielding

$$g(t) = \frac{S(0,t) + \tfrac{1}{2}V^2 S(2\pi/\mathbf{P}_{ew}, t)}{1 + \tfrac{1}{2}V^2}. \tag{41}$$

When bleached molecules do not exchange with the solution ($k_{on} \gg k_{off}$), $S(q,t)$ reduces to the exponential factor in Eq. 35b (see reference 28).

Application to experimental verification of evanescent field polarizations

Evanescent waves are predicted to have unusual polarization properties (Eqs. 14). These polarization properties allow measurement of unique characteristics of the orientation distributions of adsorbed fluorescent molecules (10–14) and may be useful for investigating anisotropic rotational motions of adsorbed fluorescent molecules (11). Although such measurements require a quantitative understanding of the evanescent field polarization, the theoretical polarization expressions (Eqs. 14) are not readily verified experimentally. In this section, the interference results are used to design two possible experimental tests of the predicted polarization properties of evanescent fields.

One method of confirming the theoretically predicted evanescent field polarizations might be measurement of the spatially averaged intensity of an evanescent interference pattern generated by fluorescent molecules at $z = 0$ whose spatial distribution and orientation are random. Specifically, assume that two beams of equal amplitudes and incidence angles are incident on such a sample. Then if one incident beam is either s-polarized ($\alpha_1 = 90°$) or p-polarized ($\alpha_1 = 0°$), and the polarization angle α_2 of the other is rotated through all possible values, the spatially averaged intensity will vary with α_2 as (Eqs. 31b)

$$I^a_{s,p} \propto 1 - \sigma_{s,p}(\theta) \sin^2 \alpha_2, \tag{42}$$

where

$$\sigma_s(\theta) = \frac{a_x^2(\theta) - a_y^2(\theta) + a_z^2(\theta)}{a_x^2(\theta) + a_y^2(\theta) + a_z^2(\theta)} \tag{43a}$$

$$\sigma_p(\theta) = \frac{a_x^2(\theta) - a_y^2(\theta) + a_z^2(\theta)}{2[a_x^2(\theta) + a_z^2(\theta)]}. \tag{43b}$$

Eq. 42 shows that one experimental test of the predicted polarization properties of evanescent fields would be verification of the $\sin^2 \alpha_2$ dependence of the spatially averaged intensity. In addition, the θ dependence of σ_s and σ_p could be measured and the results compared with theory. As shown in Fig. 6, for a quartz/air interface, the values of σ_s and σ_p should be measurable. Such data would need to be corrected for polarization-sensitive collection and detection efficiencies (29).

Another method of confirming the predicted polarizations might be measurement of visibilities, as illustrated in Fig. 4. For example, again assume that both incident beams have equal amplitudes and incidence angles. Then for s-polarized light the plane and evanescent wave visibilities are equal, and V_s thus does not manifest any of the unusual polarization properties of evanescent fields. However, for p-polarized light the plane and evanescent wave visibilities differ, and in particular, the contribution to V_p that arises from the incidence angle at higher collision angles is unique to evanescent waves. Thus, a second experimental test of the predicted polarization properties would be verification of the θ and ϕ dependence of V_p. As shown in Fig. 4, such an effect should be measurable.

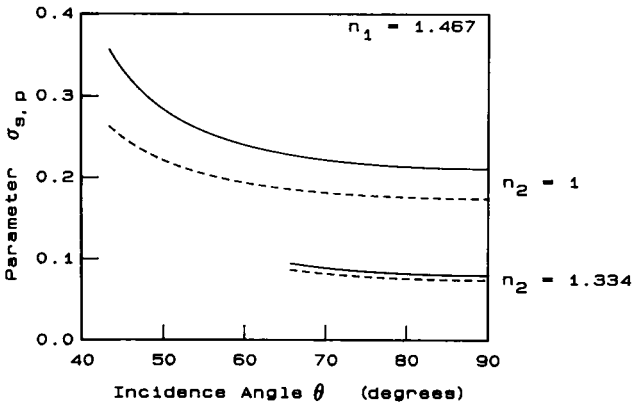

FIGURE 6 Dependence of the parameters σ_s and σ_p on the incidence angle θ. Plots are for incident beams of equal amplitudes and incidence angles θ. The variations σ_s (*solid*) and σ_p (*dashed*) in the average intensity of an evanescent interference pattern depend on θ and the polarization of the other beam (s, p). Curves were calculated from Eqs. 43 and 14 d–f using $n_1 = 1.467$ and $n_2 = 1$ (air, *top*), and $n_2 = 1.334$ (water, *bottom*).

SUMMARY

Previous experimental work has demonstrated that spatially periodic intensity patterns are generated by interfering evanescent fields. In this paper, a general theoretical description of the shapes of evanescent interference patterns has been developed. The theory provides a basis for experimentally optimizing the TIR/FPPR technique and for quantitatively analyzing TIR/FPPR data. Experiments in which the characteristics of evanescent interference patterns might be used to confirm previous theoretical predictions for evanescent field polarizations have also been described. The theoretical results for evanescent interference patterns obtained here may also be applicable in spectral regions other than the visible.

We thank Daniel Axelrod of the University of Michigan for helpful comments.

This work was supported by National Institutes of Health grant GM-37145 to Dr. Thompson and by a Camille and Henry Dreyfus Foundation Teacher-Scholar Award also to Dr. Thompson.

Received for publication 13 May 1991 and in final form 10 October 1991.

REFERENCES

1. Axelrod, D., T. P. Burghardt, and N. L. Thompson. 1984. Total internal reflection fluorescence. *Annu. Rev. Biophys. Bioeng. 13:* 247–268.
2. Mahan, A. I., and C. V. Bitterli. 1978. Total internal reflection: a deeper look. *Applied Optics.* 17:509–519.
3. Hellen, E. H., R. M. Fulbright, and D. Axelrod. 1988. Total internal reflection fluorescence: theory and applications at biosurfaces. *In* Spectroscopic Membrane Probes. L. M. Loew, editor, CRC Press, Boca Raton, FL. 47–79.
4. Axelrod, D. 1981. Cell-substrate contacts illuminated by total internal reflection fluorescence. *J. Cell. Biol.* 89:141–145.
5. Lanni, F., A. S. Waggoner, and D. L. Taylor. 1985. Structural organization of interphase 3T3 fibroblasts studied by total internal reflection fluorescence microscopy. *J. Cell. Biol.* 100: 1091–1102.
6. Pisarchick, M. L., and N. L. Thompson. 1990. Binding of a monoclonal antibody and its Fab fragment to supported phospholipid monolayers measured by total internal reflection fluorescence microscopy. *Biophys. J.* 58:1235–1249.
7. Poglitsch, C. L., M. T. Sumner, and N. L. Thompson. 1991. Binding of IgG to moFcγRII purified and reconstituted into supported planar membranes as measured by total internal reflection fluorescence microscopy. *Biochemistry.* 30:6662–6671.
8. Kalb, E., J. Engel, and L. K. Tamm. 1990. Binding of proteins to specific target sites in membranes measured by total internal reflection microscopy. *Biochemistry.* 29:1607–1613.
9. Sui, S., T. Uromow, and E. Sackmann. 1988. Interaction of insulin receptors with lipid bilayers and specific and nonspecific binding of insulin to supported membranes. *Biochemistry.* 27:7463–7469.
10. Hlady, V., J. Rickel, and J. D. Andrade. 1988/1989. Fluorescence of adsorbed protein layers. II. Adsorption of human lipoproteins studied by total internal reflection intrinsic fluorescence. *Colloids Surfaces.* 34:171–183.
11. Darst, S. A., C. R. Robertson, and J. A. Berzofsky. 1988. Adsorption of the protein antigen myoglobin affects the binding of conformation-specific monoclonal antibodies. *Biophys. J.* 53:533–539.
12. Thompson, N. L., H. M. McConnell, and T. P. Burghardt. 1984. Order in supported phospholipid monolayers detected by the dichroism of fluorescence excited with polarized evanescent illumination. *Biophys. J.* 46:739–747.
13. Timbs, M. M., and N. L. Thompson. 1990. Slow rotational mobilities of antibodies and lipids associated with substrate-supported phospholipid monolayers as measured by polarized fluorescence photobleaching recovery. *Biophys. J.* 58:413–428.
14. Fraaije, J. G. E. M., J. M. Lleijn, M. Van der Graaf, and J. C. Dijt. 1990. Orientation of adsorbed cytochrome *c* as a function of the electrical potential of the interface studied by total internal reflection fluorescence. *Biophys. J.* 57:965–975.
15. Burghardt, T. P., and D. Axelrod. 1983. Total internal reflection fluorescence study of energy transfer in surface-adsorbed and dissolved bovine serum albumin. *Biochemistry.* 22:979–985.
16. Burghardt, T. P., and D. Axelrod. 1981. Total internal reflection/fluorescence photobleaching recovery study of serum albumin adsorption dynamics. *Biophys. J.* 33:455–467.
17. Burghardt, T. P., and N. L. Thompson. 1984. Evanescent intensity of a focused Gaussian light beam undergoing total internal reflection in a prism. *Opt. Eng.* 23:62–67.
18. Axelrod, D., R. M. Fulbright, and E. H. Hellen. 1986. Adsorption kinetics on biological membranes: measurement by total internal reflection fluorescence. *In* Applications of Fluorescence in the Biomedical Sciences. D. L. Taylor, A. S. Waggoner, F. Lanni, R. F. Murphy, and R. Birge, editors. Alan R. Liss, New York. 461–476.

19. Zimmerman, R. M., C. F. Schmidt, and H. E. Gaub. 1990. Absolute quantities and equilibrium kinetics of macromolecular adsorption measured by fluorescence photobleaching in total internal reflection. *J. Colloid Interface Sci.* 139:268–280.

20. Schmidt, C. F., R. M. Zimmerman, and H. E. Gaub. 1990. Multilayer adsorption of lysozyme on a hydrophobic substrate. *Biophys. J.* 57:577–588.

21. Tilton, R. D., A. P. Gast, and C. R. Robertson. 1990. Surface diffusion of interacting proteins: effect of concentration on the lateral mobility of adsorbed bovine serum albumin. *Biophys. J.* 58:1321–1326.

22. Tilton, R. D., C. R. Robertson, and A. P. Gast. 1990. Lateral diffusion of bovine serum albumin adsorbed at the solid-liquid interface. *J. Colloid Interface Sci.* 137:192–203.

23. Weis, R. M., K. Balakrishnan, B. A. Smith, and H. M. McConnell. 1982. Stimulation of fluorescence in a small contact region between rat basophil leukemia cells and planar lipid membrane targets by coherent evanescent radiation. *J. Biol. Chem.* 257:6440–6445.

24. Born, M., and E. Wolf. 1980. Principles of Optics, 6th ed. Pergamon, New York. 808 pp.

25. Axelrod, D., D. E. Koppel, J. Schlessinger, E. Elson, and W. W. Webb. 1976. Mobility measurement by analysis of fluorescence photobleaching recovery kinetics. *Biophys. J.* 16:1055–1069.

26. Davoust, J., P. F. Devaux, and L. Leger. 1982. Fringe pattern photobleaching, a new method for the measurement of transport coefficients of biological macromolecules. *EMBO (Eur. Mol. Biol. Organ.) J.* 1:1233–1238.

27. Smith, B. A., and H. M. McConnell. 1978. Determination of molecular motion in membranes using periodic pattern photobleaching. *Proc. Natl. Acad. Sci. USA.* 75:2759–2763.

28. Thompson, N. L., T. P. Burghardt, and D. Axelrod. 1981. Measuring surface dynamics of biomolecules by total internal reflection fluorescence with photobleaching recovery or correlation spectroscopy. *Biophys. J.* 33:435–454.

29. Axelrod, D. 1989. Fluorescence polarization microscopy. *Methods Cell Biol.* 30:333–352.